Zero-shot 3D Segmentation of Abdominal Organs in CT Scans Using Segment Anything Model 2: Adapting Video Tracking Capabilities for 3D Medical Imaging

Yosuke Yamagishi, MD¹*, Shouhei Hanaoka, MD, PhD^{1,2}, Tomohiro Kikuchi, MD, MPH, PhD^{3,4}, Takahiro Nakao, MD, PhD⁴, Yuta Nakamura, MD, PhD⁴, Yukihiro Nomura, PhD^{4,5}, Soichiro Miki, MD, PhD⁴, Takeharu Yoshikawa, MD, PhD⁴, Osamu Abe, MD, PhD^{1,2}

- 1. Division of Radiology and Biomedical Engineering, Graduate School of Medicine, The University of Tokyo
- 2. Department of Radiology, The University of Tokyo Hospital
- 3. Department of Radiology, School of Medicine, Jichi Medical University
- 4. Department of Computational Diagnostic Radiology and Preventive Medicine, The University of Tokyo Hospital
- 5. Center for Frontier Medical Engineering, Chiba University

Abstract

Purpose:

This study aimed to evaluate the zero-shot performance of Segment Anything Model 2 (SAM 2) in 3D segmentation of abdominal organs in CT scans, leveraging its video tracking capabilities for volumetric medical imaging.

Materials and Methods:

Using a subset of the TotalSegmentator CT dataset (n=123) from 8 different institutions, we assessed SAM 2's ability to segment 8 abdominal organs. Segmentation was initiated from three different Z-coordinate levels (caudal, mid, and cranial levels) of each organ. Performance was measured using the Dice similarity coefficient (DSC). We also analyzed organ volumes to contextualize the results.

Results:

As a zero-shot approach, larger organs with clear boundaries demonstrated high segmentation performance, with mean(median) DSCs as follows: liver 0.821(0.898), left kidney 0.870(0.921), right kidney 0.862(0.935), and spleen 0.891(0.932). Smaller or less defined structures showed lower performance: gallbladder 0.531(0.590), pancreas 0.361(0.359), and adrenal glands 0.203-0.308(0.109-0.231). Significant differences in DSC were observed depending on the starting initial slice of segmentation for different organs. A moderate positive correlation was observed between volume size and DSCs (Spearman's $r_s = 0.731$, P < .001 at caudal-level). DSCs exhibited high variability within organs, ranging from near 0 to almost 1.0, indicating substantial inconsistency in segmentation performance between scans.

Conclusion:

SAM 2 demonstrated promising zero-shot performance in segmenting certain abdominal organs in CT scans, particularly larger organs with clear boundaries. The model's ability to segment previously unseen targets without additional training highlights its potential for cross-domain generalization in medical imaging. However, improvements are needed for smaller and less defined structures.

^{*} yamagishi-yosuke0115@g.ecc.u-tokyo.ac.jp

Introduction

Medical image segmentation is a critical task in radiology, playing a vital role in diagnosis, treatment planning, and clinical research (1,2). Traditionally, this process has been labor-intensive, requiring manual delineation by skilled radiologists. However, recent advancements in deep learning have revolutionized this field, dramatically expanding the scope of automated analysis and significantly enhancing performance across diverse medical imaging tasks.

The Segment Anything Model (SAM), introduced by Meta AI, represented a significant leap forward in image segmentation technology (3). Trained on over a billion masks, SAM demonstrated remarkable versatility in segmenting a wide array of objects across various domains. SAM's zero-shot performance - its ability to segment objects it has never seen during training - in medical images has been extensively evaluated (4,5), and specialized models such as MedSAM (6), which underwent additional training for medical imaging applications, have been introduced. These developments have demonstrated SAM's potential as a promising model in radiological domains, including CT and MRI. However, SAM was primarily designed for 2D image segmentation, which imposed inherent limitations on its direct applicability to 3D volumetric data.

The release of SAM 2 in July 2024 has extended these capabilities to video segmentation (7), opening new possibilities for application in medical imaging, particularly in the analysis of 3D volumetric data such as CT scans. While SAM 2 was not specifically designed for medical applications, its zero-shot ability presents an intriguing opportunity for adaptation to medical imaging tasks. The model's video tracking capabilities suggest a novel approach to 3D medical image segmentation, treating volumetric scans as sequences of 2D slices analogous to video frames. This approach could potentially overcome limitations of traditional 3D segmentation methods, which often require extensive training on domain-specific datasets.

Although SAM 2's performance in surgical video segmentation, such as EndoVIS (8), has already been evaluated, and models like Medical SAM2 (which underwent additional training for medical applications) were released shortly after SAM 2's debut (9), the zero-shot performance of SAM 2 on the most common radiological imaging modalities, such as CT scans, remains unexplored. We chose to conduct a zero-shot evaluation rather than using models with additional training, as this approach allows us to demonstrate SAM 2's potential adaptability to completely unfamiliar medical images, providing a more robust assessment of its true capabilities in this domain.

In this study, we explore the application of SAM 2 to multi-organ segmentation in CT imaging, focusing on abdominal scans. By leveraging SAM 2's video tracking capabilities and adapting them to the context of 3D medical volumes, we aim to evaluate the model's performance in segmenting various abdominal organs across multi-center CT scans. This investigation not only assesses the potential of SAM 2 in medical imaging but also explores a new paradigm for 3D segmentation that could significantly impact clinical practice and research in radiology.

Materials and Methods

This study was conducted as a retrospective study. Importantly, because the study utilized an open dataset, approval from the institutional review board was not required. This study adheres to the guidelines set forth in the Checklist for Artificial Intelligence in Medical Imaging (CLAIM):

2024 Update, ensuring transparency and reproducibility in our AI-based medical imaging research (10).

Dataset and Preprocess Description

We aimed to evaluate the segmentation performance of major organs within the imaging range of abdominal CT, one of the most common medical imaging modalities. To conduct this performance evaluation, we utilized a subset of the TotalSegmentator CT dataset version 1.0 (11).

The TotalSegmentator dataset is a large-scale, multi-organ segmentation dataset collected from multiple institutions. We chose this dataset due to its comprehensive nature, including numerous segmentation masks for individual organs and metadata providing information on the scanning institution for each case. For our study, we specifically selected cases that included the abdominal region, excluding CT angiography scans. To ensure representation from all 8 institutions while managing the dataset size, we implemented a sampling strategy. We set a maximum of 20 cases per institution and randomly selected cases. This resulted in 20 cases each from 5 institutes, and all available cases (5, 5, and 13 respectively) from the remaining 3 institutes, totaling 123 cases. The dataset selection process is detailed in Figure 1.

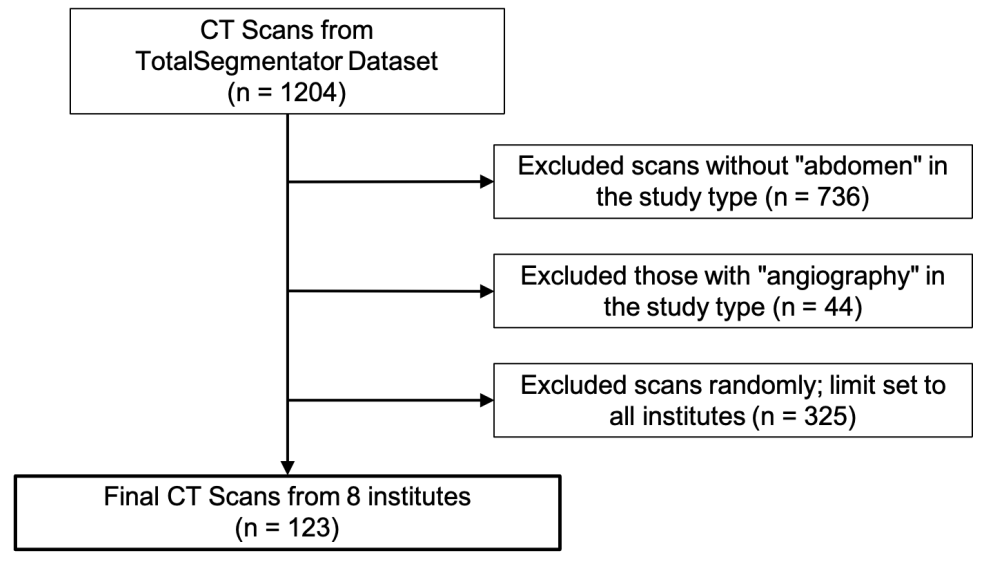


Figure 1: Flow diagram illustrating the CT scan selection process from the TotalSegmentator dataset for evaluation of SAM 2.

The average age of the patients in our selected sample was 60.7 years (standard deviation [SD] 15.5), with a gender distribution of 63 males and 60 females.

From the comprehensive organ segmentations available in TotalSegmentator, we focused on 8 major abdominal organs for our analysis:

- 1. Liver
- 2. Right Kidney
- 3. Left Kidney
- 4. Spleen
- 5. Gallbladder

- 6. Pancreas
- 7. Right Adrenal Gland
- 8. Left Adrenal Gland

These organs were chosen based on their clinical significance and visibility in standard abdominal CT scans.

The dataset is available in the NIfTI file format. For SAM 2 inference, we extracted each horizontal slice from the 3D volumes to create subsets of 2D images for each scan. Additionally, we applied windowing to the CT values, using a window level of 50 and a window width of 400 Hounsfield units, which are commonly used for abdominal CT. During model inference, we also cropped the input to focus only on the upper abdomen, intending to accelerate the inference process.

Analysis of Organ Mask Volumes and Areas

To provide context for our segmentation results and investigate the relationship between organ size and segmentation performance, we conducted two analyses: first, a volumetric analysis of organ masks, and second, an analysis of cross-sectional areas along the z-axis.

For the volumetric analysis, we utilized the existing segmentation masks from the TotalSegmentator dataset to calculate the volume of each organ in voxels. We chose to measure in voxels rather than physical units because our model inputs do not consider voxel scale.

Additionally, we analyzed cross-sectional areas of organ masks along the cranio-caudal axis. For each organ, we calculated mean mask areas at the 25th, 50th, and 75th percentile Z-coordinates, corresponding to the initial prompt locations used in SAM 2 segmentation.

SAM 2 Implementation for 3D Medical Image Segmentation

SAM 2 are segmentation models not specifically designed for medical images, but rather for general images such as portraits and landscapes. These models are trained on a large dataset, enabling them to perform segmentation on any objects. SAM 2's main feature is its ability to support not only 2D images but also videos. By inputting coordinates indicating the target object for segmentation, SAM 2 can track and segment objects appearing within the video. An overview of CT volume segmentation using SAM 2's video predictor is shown in Figure 2.

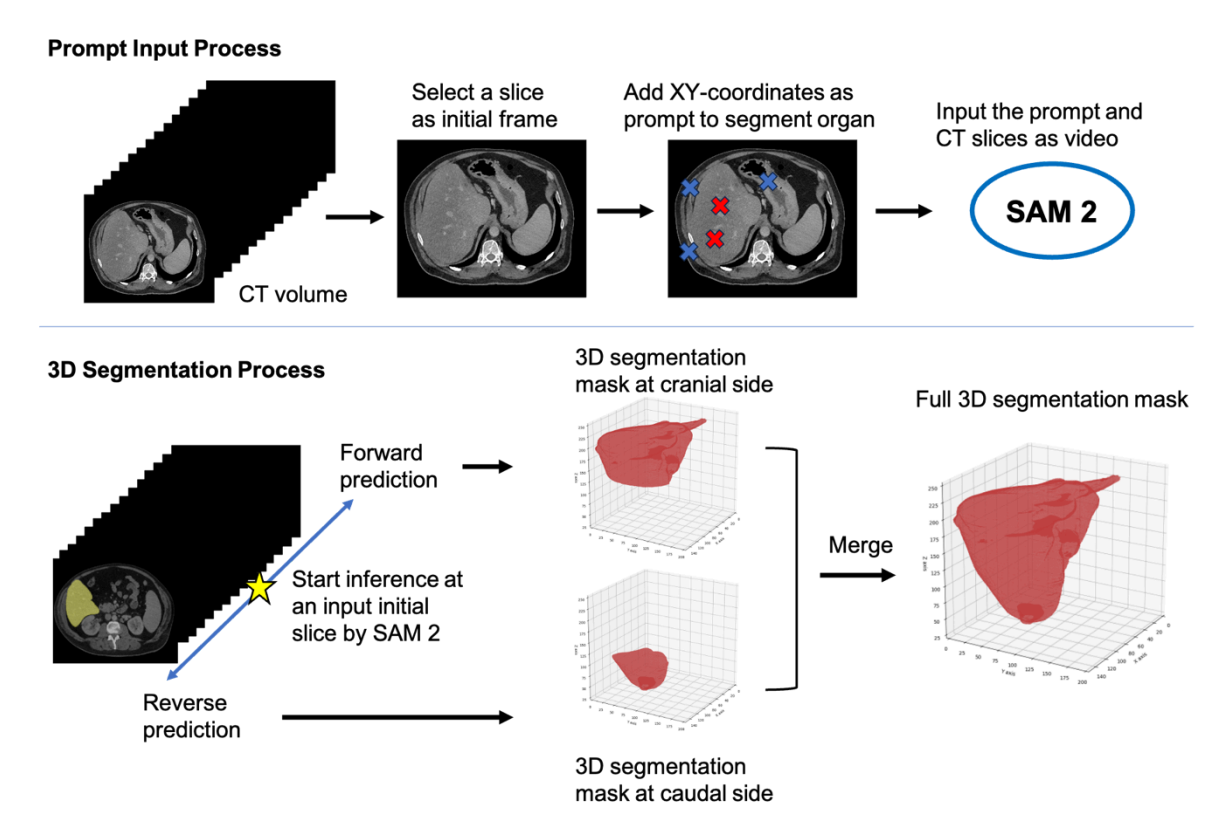


Figure 2: Workflow of 3D Medical Image Segmentation Using SAM 2. This figure illustrates a two-stage process for 3D medical image segmentation. The top row shows the Prompt Input Process, where a slice is selected from a CT volume as an initial frame, and XY-coordinates are added as prompts for organ segmentation (red crosses: positive prompts, blue crosses: negative prompts). These are then input into SAM 2. The bottom row depicts the 3D Segmentation Process, where SAM 2 performs forward and reverse predictions to generate 3D segmentation masks at both cranial and caudal sides. These masks are ultimately merged to create a full 3D segmentation mask of the target organ.

- Adaptation for 3D Medical Imaging

Although SAM 2 was originally intended for tracking objects in general videos, we recognized that 3D volumes like CT and MRI scans can be considered as videos composed of numerous 2D images. Utilizing publicly available datasets with segmentation masks, we applied preprocessing compatible with SAM 2's video prediction capabilities. This allowed us to construct a pipeline capable of performing multi-organ segmentation in a zero-shot manner, without additional training of SAM 2.

- Bidirectional Prediction Approach

SAM 2's video prediction is unidirectional. To obtain a complete segmentation mask for the entire volume, we implemented a simple bidirectional approach: the combination of forward and reverse predictions. By this approach, we were able to generate a comprehensive segmentation mask for the entire 3D volume.

- Model Inference and Prompt Setting

SAM 2's video prediction requires input of both the video (numbered 2D images) and prompt (coordinates for the target object). In practice, the prompt must be manually specified by a user. However, given the need to evaluate a large number of objects, we devised an algorithm to automatically obtain prompts:

- 1. Z-coordinate focus: Using 25th (caudal-level), 50th (mid-level), and 75th percentiles (cranial-level) for comprehensive organ representation.
- 2. Random selection within organ boundaries:
 - Five positive prompts from within the segmentation mask
 - Five negative prompts from slightly expanded area outside the mask

This method maintains reproducibility, reduces bias from the user's prompting skill, and leverages SAM 2's capability to use both positive and negative prompts for improved accuracy.

In this study, we refer to the 3D segmentations initiated from each of these positions as caudal-approach, mid-approach, and cranial-approach, corresponding to segmentations starting from the caudal, mid, and cranial-level slices, respectively.

- Model Version

For our study, we selected the "sam2_hiera_large" model, due to its highest performance among the available versions. We used version 1.0 of the SAM 2 (https://github.com/facebookresearch/segment-anything-2). Our implementation was carried out using Python 3.10.12.

Statistical Analysis:

To evaluate the model's performance, we calculated the Dice similarity coefficient (DSC). This evaluation was performed organ-wise across the dataset to provide a detailed analysis.

We compared the segmentation performance across the different approaches. For this comparison, we used the Wilcoxon signed-rank test. We performed three pairwise comparisons: caudal-approach vs mid-approach, caudal-approach vs mid-approach, and mid-approach vs cranial-approach. To account for multiple comparisons, we applied the Bonferroni correction. After Bonferroni correction, a P value <0.05/3 (approximately 0.0167) was considered statistically significant.

All statistical analyses were conducted using SciPy version 1.14.0.

Results

Analysis of Organ Mask Volumes and Areas

Organ volumes were detailed in Table 1, measured in voxels. The liver was the largest organ, followed by the spleen. Kidneys were the next largest, with similar volumes for left and right. Compared to the liver's mean volume, the pancreas was approximately 1/25, the gallbladder less than 1/70, and both adrenal glands less than 1/400 in size. These latter organs (pancreas, gallbladder, and adrenal glands) can be categorized as small organs.

We found that some organs had masks consisting of only a few voxels. We decided to use only organs with more than 100 voxels due to unreliability, which resulted in the exclusion of 12 organs in total. Consequently, a total of 891 organs from 123 CT scans were ultimately included in the evaluation.

organ	mean	median	std	min	max	n
Liver	465,008.60	440,518	156,091.00	19,768	963,401	119
Right Kidney	39,381.57	42,008	18,122.20	216	79,713	108
Left Kidney	41,246.74	42,618	21,144.60	666	129,706	111
Spleen	71,730.34	59,338.5	45,884.40	13,818	303,676	115
Gallbladder	6,247.61	6,018	4,902.72	170	20,763	89
Pancreas	18,526.41	19,626	8,502.56	707	37,855	116
Right Adrenal Gland	1,101.86	1,111	465.47	216	2,590	118
Left Adrenal Gland	1,259.03	1,205	522.81	135	2,977	115

Table 1: Descriptive Statistics of Organ Volumes in Voxels Derived from CT Scan Mask Volumes. The table presents the statistics (mean, standard deviation, median, minimum, maximum, and number of organs) for each organ.

Analysis of organ cross-sectional areas across different levels revealed diverse trends among the eight organs studied. The liver showed the largest area, consistently increasing from caudal to cranial levels. The pancreas exhibited a steady increase in area across levels. Both adrenal glands, while being the smallest organs in the study, showed peak areas at the mid-level. Detailed area trends for all organs are presented in Supplemental Figure 1.

Segmentation Performance Across Organs and Starting Positions

We evaluated the performance for multi-organ segmentation using different starting slice positions. DSC are reported as mean(median) to reflect performance variability. All results are detailed in Table 2.

The left kidney demonstrated the best overall performance, maintaining high DSCs across all starting positions: 0.870(0.921), 0.825(0.918), and 0.808(0.912) for the caudal-approach, mid-approach, and cranial-approach, respectively. Notably, it was the only organ showing no statistically significant differences between any starting positions (all P > .0167).

The box plots (Figure 3) shows that for all organs, the highest DSCs reached above 0.8, with some approaching or nearly reaching 1.0. However, the box plots also reveal instances of very low DSC values approaching 0 across various organs and approaches, indicating significant variability in segmentation performance.

Starting slice level had a significant impact on most organs. Organs demonstrated various patterns in segmentation performance depending on the starting level. The liver showed a significant decrease in performance as the starting position moved superiorly, with DSC dropping from 0.821(0.898) with caudal-approach to 0.702(0.786) with cranial-approach (P <.01). Smaller organs or those with indistinct boundaries, such as the pancreas, adrenal glands, and gallbladder, showed the most pronounced impact of starting position. For these organs,

performance significantly decreased when changing from a caudal-approach to a cranial-approach (all P<.01).

Larger organs, such as liver, kidneys, and spleen, consistently demonstrated higher DSCs compared to smaller organs across all approaches. When considering organ volumes in detail, we calculated Spearman's correlation coefficients to examine the relationship between object volumes and DSCs. A moderate correlation was observed across all settings when using caudal-approach (r_s = 0.731, P<.01), mid-approach (r_s = 0.698, P<.01), and cranial-approach (r_s = 0.699, P<.01) (12,13). As shown in Table 3, when correlation coefficients were calculated separately for each organ, fair correlations were demonstrated for almost all items, particularly in smaller organs.

organ	approach	mean	median	std	min	max	<i>P</i> value	
Liver	caudal	0.821	0.898	0.192	0.016	0.971	caudal vs mid: <.01 caudal vs cranial: <.01 mid vs cranial: 0.07	
	mid	0.754	0.860	0.223	0.186	0.966		
	cranial	0.702	0.786	0.259	0.053	0.970		
Right Kidney	caudal	0.862	0.919	0.189	0.018	0.977	caudal vs mid: 0.03 caudal vs cranial: 0.16 mid vs cranial: <.01	
	mid	0.862	0.935	0.212	0.017	0.974		
	cranial	0.801	0.918	0.270	0.000	0.964		
Left Kidney	caudal	0.870	0.921	0.154	0.000	0.968	caudal vs mid: 0.40 caudal vs cranial: 0.15	
	mid	0.825	0.918	0.221	0.003	0.973		
	cranial	0.808	0.912	0.242	0.000	0.966	mid vs cranial: 0.15	
Spleen	caudal	0.891	0.932	0.131	0.008	0.981	caudal vs mid: <.01	
	mid	0.839	0.918	0.187	0.130	0.980	caudal vs cranial: 0.0170	
	cranial	0.768	0.928	0.302	0.025	0.982	mid vs cranial: 0.56	
Gallbladder	caudal	0.527	0.547	0.288	0.001	0.939	caudal vs mid: 0.95 caudal vs cranial: <.01 mid vs cranial: 0.08	
	mid	0.531	0.590	0.291	0.000	0.947		
	cranial	0.461	0.489	0.314	0.000	0.937		
Pancreas	caudal	0.353	0.371	0.168	0.004	0.851	caudal vs mid: 0.92 caudal vs cranial: <.01 mid vs cranial: <.01	
	mid	0.361	0.359	0.197	0.000	0.773		
	cranial	0.287	0.261	0.209	0.000	0.763		
Right Adrenal Gland	caudal	0.203	0.109	0.222	0.000	0.849	caudal vs mid: <.01	
	mid	0.177	0.067	0.235	0.000	0.858	caudal vs cranial: <.01 mid vs cranial: <.01	
	cranial	0.112	0.038	0.178	0.000	0.798		
Left Adrenal Gland	caudal	0.308	0.231	0.234	0.002	0.844	caudal vs mid: <.01 caudal vs cranial: <.01	
	mid	0.252	0.174	0.226	0.000	0.805		
	cranial	0.226	0.107	0.238	0.000	0.859	mid vs cranial: 0.08	

Table 2: DSCs for multi-organ segmentation by different approaches (caudal, mid, and cranial). The table presents the statistics (mean, standard deviation, median, minimum, and maximum) for each organ by different approaches. P values from Wilcoxon signed-rank tests are provided for comparisons between approaches (caudal vs mid, caudal vs cranial, and mid vs cranial).

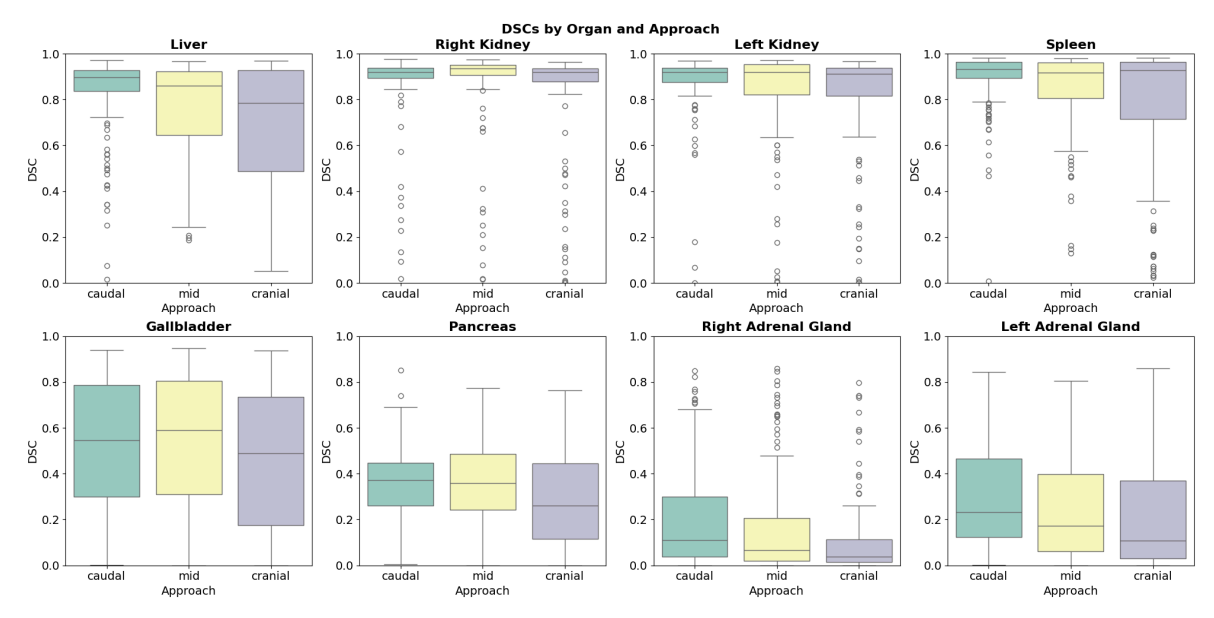


Figure 3: Box plots of DSCs for eight organs (displayed in separate subplots) across three approaches: caudal-approach, mid-approach, and cranial-approach. Each subplot shows the distribution of Dice scores (y-axis, range 0-1) for a specific organ, with the three approaches compared along the x-axis.

organ	r _s (caudal)	r _s (mid)	r _s (cranial)
Liver	0.328 (P<.01)	0.0489 (P = 0.597)	$0.163 \ (P = 0.0757)$
Right Kidney	$0.231 \ (P = 0.0164)$	0.347 (P<.01)	0.509 (P<.01)
Left Kidney	-0.0107 (P = 0.912)	0.293 (P<.01)	0.295 (P<.01)
Spleen	0.38 (P<.01)	0.307 (P<.01)	0.355 (P<.01)
Gallbladder	0.499 (P<.01)	0.509 (P<.01)	0.469 (P<.01)
Pancreas	0.475 (P<.01)	0.386 (P<.01)	0.379 (P<.01)
Right Adrenal Gland	0.371 (P<.01)	0.424 (P<.01)	0.278 (P<.01)
Left Adrenal Gland	0.452 (P<.01)	0.339 (P<.01)	0.447 (P<.01)

Table 3: Spearman correlation coefficients between ground truth of organ volumes and DSCs in caudal, mid, and cranial levels.

Next, in Figure 4, we show the highest DSC masks, excluding cases where the ground truth segmentations were incomplete. The highest-performing masks, as visualized, generated for each organ in 3D were nearly indistinguishable from the ground truth.



Figure 4: Successful segmentation results for eight abdominal organs. Each row shows a different organ with ground truth (left) and predicted (right) 3D masks. Values in parentheses indicate the DSC for each segmentation.

On the other hand, there were cases where the performance fluctuated significantly due to differences in the approach. We present an example of the liver segmentation results showing the huge DSC fluctuation due to the initial slice changes (Figure 5). The DSC decreased by 0.564 (from 0.924 with caudal-approach to 0.360 with cranial-approach). The 2D segmentation mask output with caudal-approach achieves nearly perfect segmentation at the initial slice. However, with cranial-approach, the output mask includes the inferior vena cava or incompletely mask the margins. For the caudal-approach output, the initial slice segmentation appears to have been easier due to clear contrast with the surroundings. For the cranial-approach, the decrease in accuracy can be attributed to the initial slice, where the boundaries between the liver, inferior vena cava, and the surrounding abdominal wall are unclear. As a result, 3D mask generation was not possible for slices caudal to the initial slice, leading to a low DSC. This suggests the importance of the initial segmentation 2D mask.

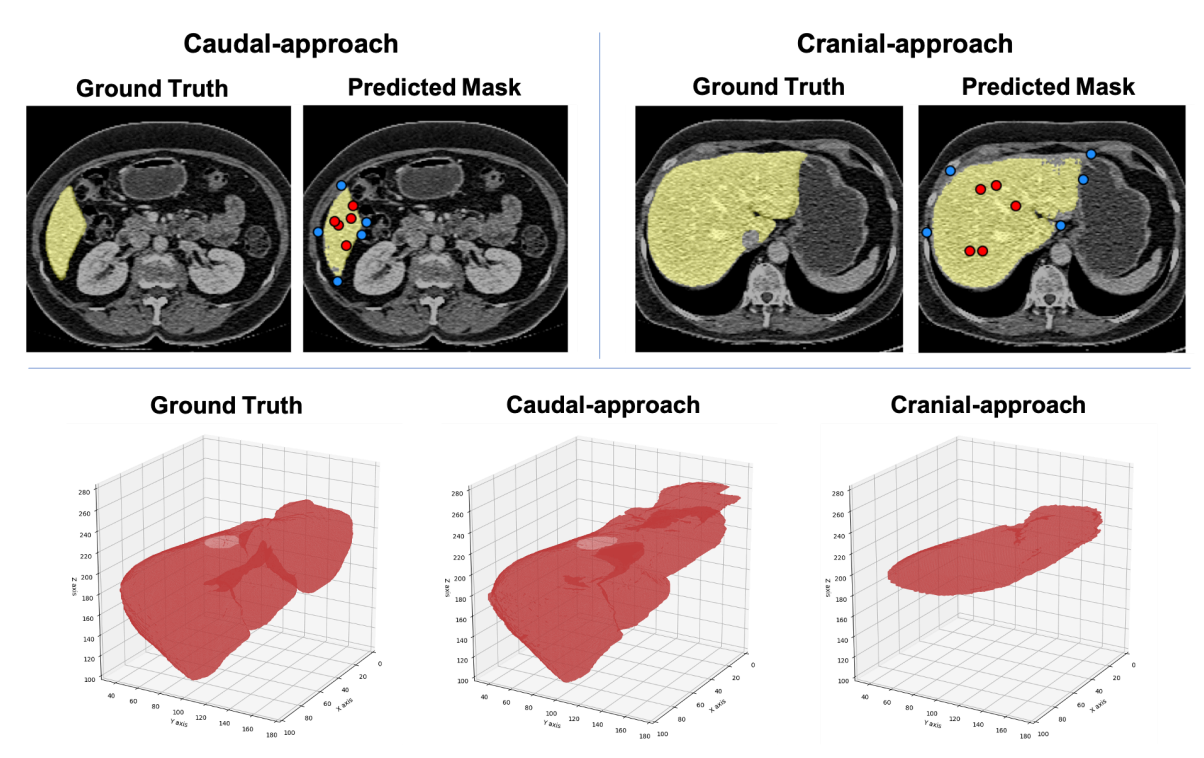


Figure 5: Comparison of segmentation results using caudal-approach and cranial-approach, showing 2D axial slices with Ground Truth and Predicted Mask for both initial slices (top row, with yellow representing the ground truth of liver, blue and red points indicating negative and positive prompts, respectively), alongside 3D renderings of liver segmentation for Ground Truth, Caudal-approach, and Cranial-approach (bottom row).

Discussion

To our knowledge, we are the first to report on zero-shot SAM 2's performance validation for radiology images. We demonstrated the potential of SAM 2, a general-purpose segmentation model, in abdominal organ segmentation from CT scans. While segmentation previously required manual annotation by radiologists, this method allows for segmentation mask

generation with just some clicks on the relevant area of a single slice.

SAM2 showed promising performance for larger organs with clear boundaries, such as the liver, kidneys, and spleen, achieving mean(median) DSC of 0.821(0.898)-0.891(0.932). This performance is noteworthy given that SAM 2 was not specifically designed for medical image analysis. In this study, we used a dataset with existing masks to validate performance. However, since these masks were unknown to SAM 2, there is potential for applying this method to any organ and lesion. While the scores are lower compared to previous supervised methods, which can achieve mean DSCs in the upper 0.9 range for some organs, they are still notably high for a zero-shot prediction. Some organs achieved median DSCs in the 0.9 range, also impressive for an unsupervised approach. While extreme outliers lowered mean scores, median values highlight the model's generally robust performance. The ability to segment an entire 3D volume by simply selecting and clicking on a target structure in a single slice is particularly significant.

The choice of initial prompt position had a significant impact on segmentation accuracy and the optimal position depended on the organ. This emphasizes that performance is highly dependent on the choice of initial slice. Segmentation performance can be inferred to depend on multiple factors related to the 3D morphology, volume size, and contrast with surrounding tissues of target structure. This finding suggests the importance of determining the initial slice taking into account the characteristics of the targeted structure.

SAM 2 struggled with smaller and less defined structures such as the adrenal glands, pancreas, and gallbladder, resulting in lower DSCs. Interestingly, we observed a moderate positive correlation between organ volume and DSCs (Spearman's $r_s = 0.731$, P < .01), suggesting that volume size is one of several key factors influencing segmentation accuracy. This aligns with challenges typically observed in abdominal organ segmentation, even with supervised 3D models. Notably, supervised approaches like TotalSegmentator (based on nnUNet (14)), UNet (15), SegUNet (16), and SwinUNETR (17) also tend to show lower DSC for bilateral adrenal glands and gallbladder compared to other organs (18), a trend mirrored in SAM 2's performance.

Our study had several limitations. Firstly, our validation dataset was limited to abdominal CT scans, one of the most standard modalities. There are publicly available datasets such as Vertebral Segmentation, TotalSegmentator's MRI and Duke Liver datasets (19–21), which include segmentation masks for various anatomical structures and modalities. Expanding our validation using these resources would allow for a more robust evaluation. Additionally, as our approach was designed to address zero-shot performance validation, we did not perform any additional training such as fine-tuning. Our method showed good performance for organs with clear boundaries like the liver and spleen, but achieved limited accuracy for smaller organs like adrenal glands. Performance improvements can be expected by using task-specific supervised methods instead of zero-shot.

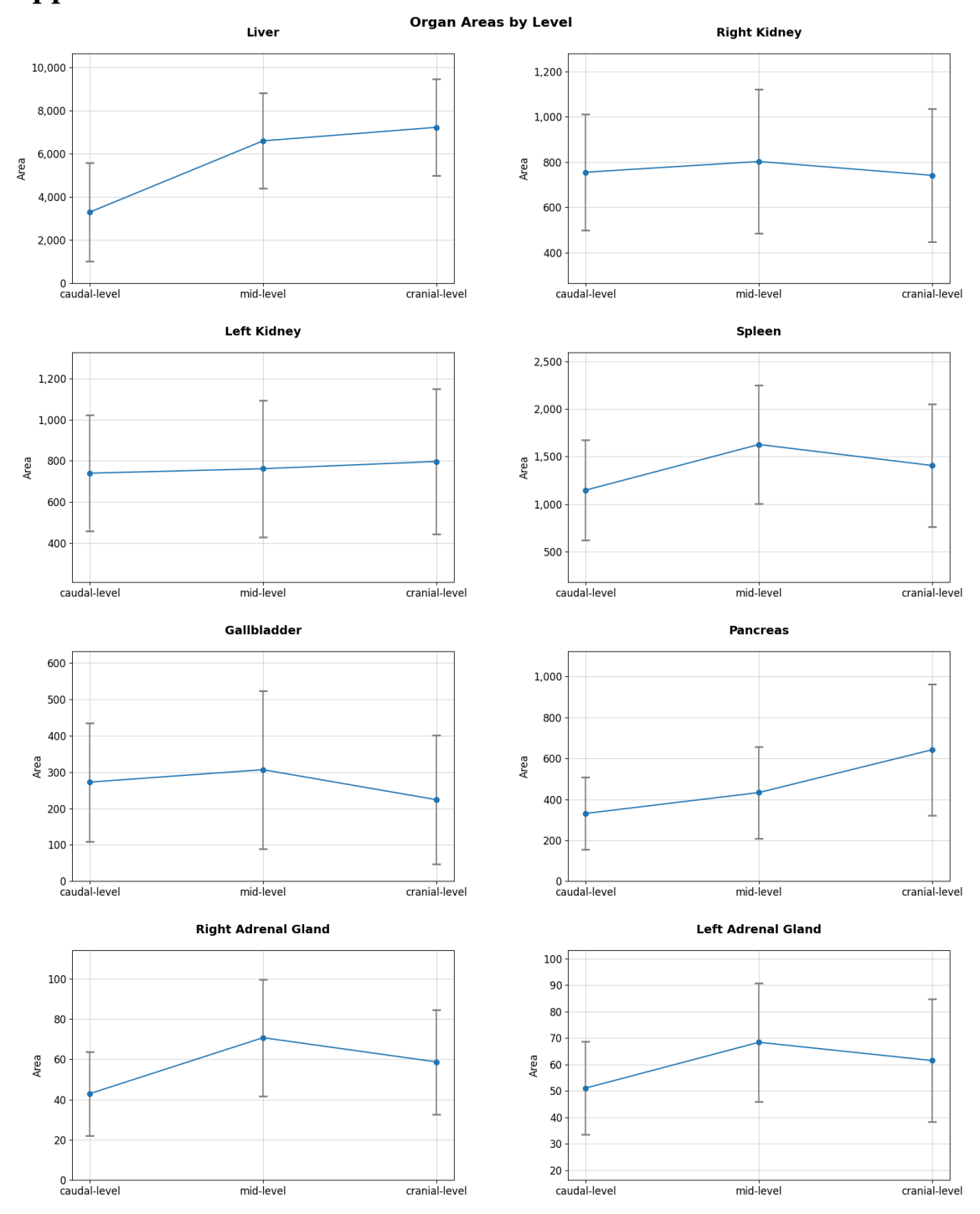
In conclusion, SAM 2 has demonstrated promising zero-shot performance in segmenting certain abdominal organs in CT scans, particularly larger organs with clear boundaries, highlighting its potential for cross-domain generalization in medical imaging. However, further improvements are needed for smaller and less distinct structures. Our study underscores the importance of applying general models to completely novel data and optimizing input prompts, which together could significantly enhance the accuracy of medical image segmentation.

References

- 1. Wang S, Summers RM. Machine learning and radiology. Medical Image Analysis. 2012;16(5):933–951. doi: 10.1016/j.media.2012.02.005.
- 2. Saba L, Biswas M, Kuppili V, et al. The present and future of deep learning in radiology. European Journal of Radiology. 2019;114:14–24. doi: 10.1016/j.ejrad.2019.02.038.
- 3. Kirillov A, Mintun E, Ravi N, et al. Segment Anything. arXiv; 2023. doi: 10.48550/arXiv.2304.02643.
- 4. Mazurowski MA, Dong H, Gu H, Yang J, Konz N, Zhang Y. Segment anything model for medical image analysis: An experimental study. Medical Image Analysis. 2023;89:102918. doi: 10.1016/j.media.2023.102918.
- 5. Roy S, Wald T, Koehler G, et al. SAM.MD: Zero-shot medical image segmentation capabilities of the Segment Anything Model. arXiv; 2023. doi: 10.48550/arXiv.2304.05396.
- 6. Ma J, He Y, Li F, Han L, You C, Wang B. Segment anything in medical images. Nat Commun. Nature Publishing Group; 2024;15(1):654. doi: 10.1038/s41467-024-44824-z.
- 7. Ravi N, Gabeur V, Hu Y-T, et al. SAM 2: Segment Anything in Images and Videos. arXiv; 2024. http://arxiv.org/abs/2408.00714. Accessed August 2, 2024.
- 8. Allan M, Kondo S, Bodenstedt S, et al. 2018 Robotic Scene Segmentation Challenge. arXiv; 2020. doi: 10.48550/arXiv.2001.11190.
- 9. Zhu J, Qi Y, Wu J. Medical SAM 2: Segment medical images as video via Segment Anything Model 2. arXiv; 2024. http://arxiv.org/abs/2408.00874. Accessed August 7, 2024.
- 10. Tejani AS, Klontzas ME, Gatti AA, et al. Checklist for Artificial Intelligence in Medical Imaging (CLAIM): 2024 Update. Radiology: Artificial Intelligence. Radiological Society of North America; 2024;6(4):e240300. doi: 10.1148/ryai.240300.
- 11. Wasserthal J, Breit H-C, Meyer MT, et al. TotalSegmentator: Robust Segmentation of 104 Anatomic Structures in CT Images. Radiol Artif Intell. 2023;5(5):e230024. doi: 10.1148/ryai.230024.
- 12. Akoglu H. User's guide to correlation coefficients. Turk J Emerg Med. 2018;18(3):91–93. doi: 10.1016/j.tjem.2018.08.001.
- 13. Chan YH. Biostatistics 104: correlational analysis. Singapore Med J. 2003;44(12):614–619. Accessed August 10, 2024.
- 14. Isensee F, Jaeger PF, Kohl SAA, Petersen J, Maier-Hein KH. nnU-Net: a self-configuring method for deep learning-based biomedical image segmentation. Nat Methods. Nature Publishing Group; 2021;18(2):203–211. doi: 10.1038/s41592-020-01008-z.
- 15. Ronneberger O, Fischer P, Brox T. U-Net: Convolutional Networks for Biomedical Image Segmentation. In: Navab N, Hornegger J, Wells WM, Frangi AF, editors. Medical Image Computing and Computer-Assisted Intervention MICCAI 2015. Cham: Springer International Publishing; 2015. p. 234–241. doi: 10.1007/978-3-319-24574-4_28.
- 16. Chen X, Cheng G, Cai Y, Wen D, Li H. Semantic Segmentation with Modified Deep Residual Networks. In: Tan T, Li X, Chen X, Zhou J, Yang J, Cheng H, editors. Pattern Recognition. Singapore: Springer; 2016. p. 42–54. doi: 10.1007/978-981-10-3005-5_4.
- 17. Swin UNETR: Swin Transformers for Semantic Segmentation of Brain Tumors in MRI Images | SpringerLink. https://link.springer.com/chapter/10.1007/978-3-031-08999-2_22. Accessed August 8, 2024.
- 18. Li W, Yuille A, Zhou Z. How Well Do Supervised 3D Models Transfer to Medical Imaging

- Tasks? The Twelfth International Conference on Learning Representations. 2024. https://openreview.net/forum?id=AhizIPytk4. Accessed August 10, 2024.
- 19. Macdonald JA, Zhu Z, Konkel B, Mazurowski MA, Wiggins WF, Bashir MR. Duke Liver Dataset: A Publicly Available Liver MRI Dataset with Liver Segmentation Masks and Series Labels. Radiol Artif Intell. 2023;5(5):e220275. doi: 10.1148/ryai.220275.
- 20. Löffler MT, Sekuboyina A, Jacob A, et al. A Vertebral Segmentation Dataset with Fracture Grading. Radiol Artif Intell. 2020;2(4):e190138. doi: 10.1148/ryai.2020190138.
- 21. D'Antonoli TA, Berger LK, Indrakanti AK, et al. TotalSegmentator MRI: Sequence-Independent Segmentation of 59 Anatomical Structures in MR images. arXiv; 2024. doi: 10.48550/arXiv.2405.19492.

Supplemental Materials



Supplemental Figure 1. Comparison of organ areas across different levels. The graph displays the mean areas (in voxel) of organs at the caudal-level, mid-level, and cranial-level. Error bars represent standard deviations.